Arrangement of Inner Dynein Arms in Wild-Type and Mutant Flagella of *Chlamydomonas*

David N. Mastronarde, Eileen T. O'Toole, Kent L. McDonald, J. Richard McIntosh, and Mary E. Porter*

Laboratory for Three-dimensional Fine Structure, Department of Molecular, Cellular, and Developmental Biology, University of Colorado, Boulder, Colorado 80309-0347; and *Department of Cell Biology and Neuroanatomy, University of Minnesota School of Medicine, Minneapolis, Minnesota 55455

Abstract. We have used computer averaging of electron micrographs from longitudinal and cross-sections of wild-type and mutant axonemes to determine the arrangement of the inner dynein arms in *Chlamydomonas reinhardtii*. Based on biochemical and morphological data, the inner arms have previously been described as consisting of three distinct subspecies, I1, I2, and I3. Our longitudinal averages revealed 10 distinguishable lobes of density per 96-nm repeating unit in the inner row of dynein arms. These lobes occurred predominantly but not exclusively in two parallel rows. We have analyzed mutant strains that are missing I1 and I2 subspecies. Cross-sectional averages of *pf9* axonemes, which are missing the I1 subspecies, showed a loss of density in both the inner and outer portions of the inner arm. Averages from longitudinal images showed that three distinct lobes were missing from a single region; two of the lobes were near the outer arms but one was more inward. Serial 24-nm cross-sections of *pf9* axonemes showed a complete gap at the proximal end of the repeating unit, confirming that the I1 subunit spans both inner and outer portions of the inner arm region. Examination of *pf23* axonemes, which are missing both I1 and I2 subspecies, showed an additional loss almost exclusively in the inner portion of the inner arm. In longitudinal view, this additional loss occurred in three separate locations and consisted of three inwardly placed lobes, one adjacent to each of the two radial spokes and the third at the distal end of the repeating unit. These same lobes were absent in *ida4* axonemes, which lack only the I2 subspecies. The I2 subspecies thus does not consist of a single dynein arm subunit in the middle of the repeating unit. The radial spoke suppressor mutation, *pf2*, is missing four polypeptides of previously unknown location. Averages of these axonemes were missing a portion of the structures remaining in *pf23* axonemes. This result suggests that polypeptides of the radial spoke control system are close to the inner dynein arms.

FLAGELLAR motion is accomplished by sliding between doublet microtubules of the axoneme, mediated by the action of dynein ATPases. Dynein arms are organized in two rows. In *Chlamydomonas*, the inner row is more complex than the outer one in several respects, and there is much interest in understanding its structure and function. The importance of inner arms to flagellar function is shown by the finding that most mutants lacking outer dynein arms have motile flagella, whereas loss of most of the inner arm results in flagellar paralysis (Kamiya et al., 1989). The outer row of dynein arms follows a simple plan: there are four identical arms per 96-nm repeating unit of the axoneme (Goodenough and Heuser, 1989), each composed of three dynein heavy chains and associated intermediate and low molecular weight polypeptides (King and Witman, 1989). The biochemistry of the inner arms is more complex: six distinct dynein heavy chains have been identified, as well as associated intermediate and light polypeptides (Luck and Piperno, 1989; Piperno et al., 1990). In the terminology of Piperno et al. (1990), the heavy chains are referred to as 1α, 1β, 2', 2, 3, and 3', in order of decreasing molecular weight.

The structural organization of the inner dynein arms is disputed. Based mainly on rapid-freeze, deep-etch images of axonemes from *Tetrahymena* and *Beröe*, the model of Goodenough and Heuser (1989) shows the globular heads of the inner dynein arms mostly lined up in a single row. Moving along the axoneme from base to tip, each 96-nm repeating unit consists of a three- or four-headed arm (a triad) followed by two double-headed arms (dyads). Piperno et al. (1990) examined longitudinal sections of *Chlamydomonas* axonemes from wild-type, *pf30*, and *pf23* cells. *Pf30* is an allele at the *PF9* locus that lacks the 1α and 1β polypeptides (see companion paper, Porter et al., 1992), whereas *pf23* additionally lacks the 2,2', and 3' heavy chains. The results of Piperno et al. (1990), and evidence on variations in the composition of the inner arms with positions along the length of the axoneme (Piperno and Ramanis, 1991), led to the following model. The first inner arm, I1, proximal to radial spoke 1

(S1), is composed of the 1α and 1β heavy chains. The second inner arm, I2, is a dyad located between the two radial spokes and is formed of either the 2 or 2′ heavy chains, depending on long-range position along the axoneme. The third inner arm, I3, is a dyad distal to the second radial spoke (S2) and is formed of either the 3 or 3′ heavy chains. Kamiya et al. (1991) averaged cross-sectional views of outer doublets from wild-type, *ida1–3* (other strains that lack the 1α/1β heavy chain subunit), and the *ida4* strain, which has deficiencies in heavy chains 2 and 2′. The *ida1–3* and *ida4* strains were missing density in an outer and an inner portion of the inner arm, respectively, leading to the suggestion that inner arms are arranged in two parallel rows, with I1 situated in an outer row and I2 in an inner one. Muto et al. (1991) provided additional support for this idea by examining tilt series of longitudinal sections with wild-type inner arms. Their model shows 10 separate lobes arranged in two discrete rows.

The work we report here resolves many of the inconsistencies among the models just cited. We have applied several image averaging techniques to electron micrographs of *Chlamydomonas* axonemes in order to obtain the most reliable views of inner dynein arms that our preparative techniques would allow. Initially we used cross-sectional images to assess the structural defect in the *pf9* strain and the extent of recovery in several revertants (see accompanying paper, Porter et al., 1992). During this work, we found it necessary to develop methods not just for aligning and averaging these large structures but also for making valid comparisons between averages from different strains. These methods have provided us with more refined estimates of the locations of the I1 and I2 structures in cross-sectional view. To assess the distribution of structures in the third dimension, along the length of the repeating unit, we extended our analysis in two ways. First, we examined very thin (24-nm) serial sections of axonemes; this analysis confirmed the location of the I1 subunit in the proximal portion of the repeating unit and revealed some of the complexity in the rest of the inner arm structures. Second, we averaged images from longitudinal sections of wild-type and mutant axonemes. This work yielded a clear view of the structures present along the inner row and indicated which structures were missing in various mutant axonemes. With this combination of methods, we have thus obtained significant new information on the three-dimensional structure of the inner row of dynein arms.

Materials and Methods

Electron Microscopy

Axonemes were prepared for electron microscopy as described in Porter et al. (1992). Sections of different thicknesses were cut, depending on the type of analysis to be done: the cross-sectional averages used silver-gray sections of nominal thickness 60 nm, placed on bare 200 mesh grids; the analysis of longitudinal sections used 40-nm sections picked up on bare grids; the serial section analysis of cross-sections used 24-nm serial sections picked up on formvar-covered slot grids. The precision of the section thickness was crucial only for the serial sections; in that case, as described below, the occurrence of repeating axonemal structures every fourth section indicated that the average section thickness was indeed close to the nominal thickness of 24 nm. All sections were post-stained for 7 min in 2% aqueous uranyl acetate and 3 min in lead citrate.

All microscopy was done on a CM10 electron microscope (Philips Electronic Instruments Co.; Mahwah, NJ.) operating at 80 kV. Micrographs for both longitudinal and cross-sectional analysis were taken at a magnification of 39,000.

Microscopy and Digitization for Cross-sectional Averaging

Axonemes were selected for microscopy based on their preservation and orientation. Only axonemes that included complete outer doublet microtubules and both central pair microtubules were considered to be intact, except preparations of *pf23* in which nearly all axonemes were missing one of the central pair.

Axonemes were selected for further study if they were nearly circular and if protofilaments were visible in the walls of at least one of the doublet microtubules. Images of axonemes were digitized from the negatives using a video camera (model MTI-81; Dage-MTI Inc., Michigan City, IN) with a Saticon tube. Camera gain and black level were adjusted for each micrograph so that the range from the darkest part of the background to the brightest part of the axoneme filled the dynamic range of the digitizer. Eight successive video frames, each digitized with 6 bits of gray-scale resolution, were averaged and stored as an 8-bit number; the resulting pixel values were reproducible to ~1%. All axonemes were positioned in a standard orientation within an area of 304 × 300 pixels and digitized at a uniform scale of 0.9 nm/pixel (see Fig. 1 *A*). Digitization and analysis were performed on a MicroVAX III computer containing a Parallax 1280 videographics device (Parallax Graphics Inc., Santa Clara, CA).

Selection of Individual Doublets

The criterion for selection of outer doublets for further processing was the clarity of their protofilaments (e.g., the three doublets marked by white crosses in Fig. 1 *A*). For strains with outer arms, the few doublets that lacked the outer dynein arm were excluded, but otherwise the appearance of the dynein arms was not considered in selecting doublets. We chose at least 40, and typically 50–100, doublets for averaging from a given sample. The image of each chosen doublet was placed in a 90 × 70 pixel box. The program for this operation used the positions of all nine doublets, as marked by hand with a cursor, to determine the translations and rotations needed to place each doublet roughly into a standard orientation (see Fig. 1 *B*). Quadratic interpolation was used for this and all following image transformations.

General Alignment Procedures

When we needed to align one image to another, we usually used a general linear transformation, which involves six parameters: X and Y translation, rotation, overall magnification, and stretch along any one axis. Such a transformation can adjust for many of the distortions introduced during sectioning and microscopy. Three different methods were used to obtain such transformations. (*1*) For automatic alignment, we used a program that searched for the six transformation parameters that minimized the difference between any two images, as measured by the sum, over all pixels, of the absolute value of the differences between one image and the transformation of the other. For such an alignment, the intensities of the two images were first adjusted to have the same mean and variance. (*2*) For fiducial alignment, we used a cursor to mark the positions of six or more well-defined points that corresponded between two images. Multiple linear regression was used to solve for the six parameters of the linear transformation that would minimize the disparity between the fiducial points in the two images. Since three points provide enough information to specify a transformation, six or more points allow some averaging of the errors introduced by inaccurate cursor placement or by the failure of points to correspond exactly between images. (*3*) For manual alignment, we used a program that could rapidly present an approximate transformation of one of the images while the operator manually adjusted any of the six parameters. To judge the alignment, one could either quickly alternate between the two images shown in gray-scale, or superimpose the two, with one displayed in green and the other in magenta. Good alignment was indicated by a maximum of white in the resulting image.

Averaging Individual Doublets

In preparation for averaging, the many doublet images for a given sample were aligned by applying the automatic method in two stages. For initial alignment, images were filtered to enhance low spatial frequencies, making the walls and lumens of the A and B subfibers the dominant image features (Fig. 1 *C*). The search program was run for each filtered doublet to find the transformation that would best align it to a preexisting average of wild-type doublets. The original images were transformed and then filtered to enhance high spatial frequencies, making the protofilaments into the domi-

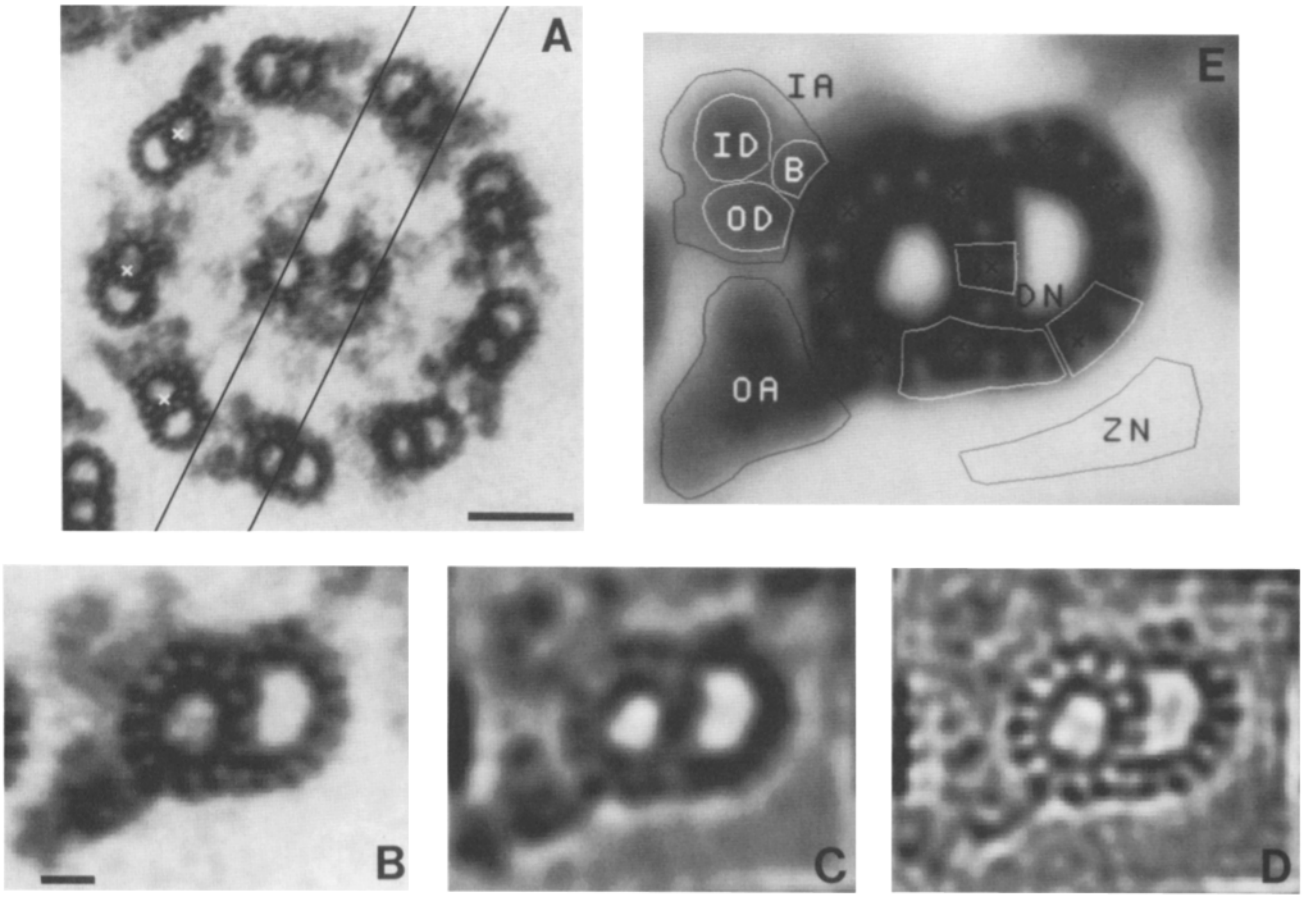

Figure 1. (*A*) Typical cross-section of a wild-type axoneme. The doublets selected for averaging are marked with white crosses. The parallel lines show the boundaries of the typical 40-nm longitudinal section suitable for imaging inner arms. Bar = 50 nm. (*B*) One doublet from that axoneme, placed into the standard 90 × 70 pixel box. (*C, D*) The doublet shown in *B* filtered for the first and second stages of alignment, respectively. Bar = 10 nm for *B–D*. (*E*) An average of images from wild-type doublets, marked to show the areas averaged in the quantitative analysis of cross-sectional averages: zero normalizing area (*ZN*), doublet normalizing areas (*DN*), outer dynein arm (*OA*), inner dynein arm (*IA*), inner domain (*ID*), outer domain (*OD*), and base (*B*).

nant image features (Fig. 1 *D*). The search program was run again to find a refining transform for each doublet. These second transforms were applied to the already-transformed doublets and the resulting images were averaged.

We found that the automatic alignment method was adequate despite its imperfections, which arise because the transformation search program is not guaranteed to find a global minimum in the image difference, and because noise in the images can lead to a suboptimal alignment. For one sample, we compared the results from our automatic alignment with those achieved with a more sophisticated approach in which we represented each doublet by a curve traced over its protofilaments in the center of the microtubule walls. A program solved for the transformations that best aligned these curves. We devised this method because it seemed likely to be the most reliable way to obtain optimal alignment of the doublet microtubules for every doublet in the sample. When the curves were transformed and superimposed, it was seen that they were indeed brought into better alignment by these solved transformations than by the automatically obtained ones; by implication, the doublet images were better aligned as well. However, the average image obtained with these transformations was no better than the standard average in two respects: the contrast of the protofilaments was not higher, and the standard deviations of intensities were not lower. Thus, there was no reason to replace automatic alignment with a slightly more reliable but labor-intensive procedure.

Final Alignment, Normalization, and Comparison of Averages

Final alignment between all of the various average images was achieved by registration of their protofilaments. This step was seen to be necessary by viewing different averages in quick succession; there were small misalignments that obviously needed to be eliminated before quantitative comparisons between images could be meaningful. This final alignment was performed by the fiducial method, using the centers of 10 of the protofilaments in the average as fiducial points (crosses in Fig. 1 *E*). All averages were aligned to a single, reference average. This procedure was quite accurate; the transformed positions of the fiducial points deviated from the positions in the reference image by an average of 0.2 pixel (0.18 nm) and by at most 0.6 pixel (0.54 nm). The alignment process thus requires three sequential transformations: the rough and fine alignment transforms for each doublet, and the overall alignment transforms for the average. To minimize the number of successive interpolations, which might degrade image quality, the alignment transforms for each doublet were numerically combined with the transform for the average to obtain a single transformation for each doublet. The doublets could thus be transformed from their original positions into their final alignment with only one interpolation step; they were then averaged without further transformations.

Because the samples varied in staining intensity, it was necessary to normalize the image intensities between different averages. Normalization was performed with a program that scaled image intensities and computed average intensities within selected areas. Regions of interest were specified by using a cursor to trace contours over an aligned, average wild-type image; Fig. 1 *E* shows the regions used here. Two regions were designated for normalizing the intensities of different averages. Intensities were shifted so that the mean of all pixels became 0 within the region marked "ZN" in Fig. 1 *E*, which corresponds to open space outside the axoneme. The intensities were then scaled so that the mean became 1 either within the regions in the microtubule walls marked "DN" in Fig. 1 *E* (to yield a "doublet-normalized" average), or within the region enclosing the outer dynein arm, marked "OA" in Fig. 1 *E* (to yield an "outer arm–normalized" average). After determining the scaling needed to normalize an average image, the program applied this

same scaling to all of the individual doublet images. The program then computed the mean intensity within specified regions of each doublet and, for each such region, it obtained both the mean and standard deviation of these means over the collection of doublets. To enable further statistical comparisons, the program also computed the standard deviation of the scaled intensities at each pixel.

When averages from two samples of the same strain are compared, they often appear slightly different. Such differences were in fact statistically significant; that is, the variability among the doublets for any one sample was not sufficient to account for variation between samples. Intersample differences may arise from differences in preparation, fixation, staining, microscopy, or digitization. Whatever their source, they demonstrate that multiple samples are needed to determine the structural phenotype of any one strain with confidence and to compare the phenotypes of different strains. An appropriate statistical model for this situation is a two-level nested analysis of variance, which allows one to evaluate the significance of variation between strains while taking into account both the variation among the doublets contributing to each sample and the variation between different samples of the same strain. All of the sums of squared deviations needed for this analysis can be computed from the means, standard deviations, and number of doublets for each sample. Programs were thus written to use the output of the image normalizing and averaging program to test for the significance of differences either between mean intensities in the specified areas or between the average images at every pixel.

Averaging of Longitudinal Sections

The first step in our analysis of longitudinal sections was to select appropriate images. Inner dynein arms were identifiable with the least ambiguity in 40-nm sections that included the central pair microtubules (see lines in Fig. 1 *A* depicting a representative section). In such a section, a doublet microtubule often appeared bare but sometimes showed associated densities. The presence of clear outer arms, with the tips of individual arms distinguishable, was taken as an indication that densities superimposed on the inner part of the doublet microtubule corresponded to inner dynein arms. We relied here on the fact that it would be very difficult for a section through the central pair to be oriented so as to retain most of the outer arms but truncate the inner arms (see Fig. 1 *A*). We selected axonemes that were as straight as possible and that appeared fairly uniform for five or more repeats of the 96-nm longitudinal unit characteristic of axonemal structure. Fig. 11 *A* shows 10 repeats from the straightest, most uniform axoneme that we found. Density corresponding to the position of the inner arm is clearly visible on both outer doublets, in the region between the outer arms (*O*) and radial spokes (*S*). In most other cases, only one of the two doublets showed clear images of inner and outer dynein arms. We thus digitized an area containing only the doublet of interest, the radial spokes, and most of the central pair.

To average the repeating structure, we marked positions in the middle of each rectangle formed by radial spokes, central pair, and outer doublet (star in Fig. 11 *A*). The image centered on each position was placed into a 168-pixel square box (1.5 repeats at 0.9 nm/pixel). These image segments were averaged and then automatically aligned to this average, allowing only rotations and translations. The aligned segments were then averaged again, the original images were aligned to this second average, and the realigned images were used to get a final average.

Because an average based on a few segments can be seriously degraded by poor alignment of only one segment, we examined the alignment of the individual segments to the average in cases involving particularly large translations or rotations. For ~10% of the averages, we used the manual alignment program to adjust the alignment of some of the segments. However, most of these adjustments did not improve the average appreciably.

All of the various longitudinal averages were aligned with each other by a two-stage procedure using the manual alignment program. In the first stage, each average was aligned to a reference image. There was a separate reference image for each strain. Initially, an individual average was used as the reference; but after grand averages became available, each individual average was realigned to one of the grand averages. In the second stage, each reference image was aligned to a "master" reference, which was an average of some preliminarily aligned grand averages. The transformations from the two stages were then combined, thus allowing each individual average to be transformed into alignment with the average reference.

Manual alignment was used because it allowed us to focus on the registration of the inner dynein arm structures, which occupied only a small part of the image area. This selective alignment was necessary because the sections containing individual axonemes were cut in such a way that the doublets were viewed at a range of slightly different orientations. This unavoidable variability made the inner arms appear at slightly different positions relative to the doublet and the outer arms. An alignment based on all structures present would thus have needlessly blurred inner arm structures. These alignments involved the adjustment of five parameters, as follows: The overall magnification was first set so that the distance spanned by the six outer arms in the average being aligned matched that in the reference. If inner arm structures in the average then appeared markedly compressed or extended in the radial direction, an appropriate stretch was imposed in that direction. Such corrections were needed primarily to compensate for distortions introduced during sectioning, as well as for the fact that inner arm structures were viewed at a range of different angles. Finally, rotation and X and Y position were adjusted to bring the inner arm structures into the best registration, while misalignments in other structures were mostly ignored. Although this procedure has a subjective element, it is difficult to see how it could produce artifacts in the final results, because the images being aligned were already averages in which the basic features being aligned were fairly well defined.

Results

Inter-Sample Variability and Outer Arm Normalization

Our initial experiments were aimed at determining the differences in the structural phenotypes between samples from wild-type cells and mutant strains that are deficient in inner arm polypeptides. While clear differences between wild-type and mutant samples could be observed, we grew concerned about whether these differences reflected true structural deficiencies or simple sample variability. To control for variations in sample preparation, we devised programs for normalizing the intensities of the various samples to a common scale. Our procedure for forming an average image emphasizes the doublet microtubules, rather than the dynein arms, for selecting and aligning individual doublets. We had hoped to use the doublet microtubules for intensity normalization as well, but this was not adequate for quantitative comparison, as illustrated by the three wild-type samples compared with doublet normalization in Fig. 2, *A–C*. Because of the normalization, the overall intensity of the microtubules is similar in the three cases; however, both the intensity of the dynein arms and the appearance of the doublets vary widely. The samples in Fig. 2, *A–C* depict typical variations in doublet appearance. In addition to variations in the distinctness of the protofilaments, some samples had broad microtubule walls and rather small openings in the centers of the subfibers (e.g., Fig. 2 *C*), while others had thinner walls and larger openings (Fig. 2, *A* and *B*); for some but not all of the latter, the protofilaments on the B subfiber lacked outer boundaries (Fig. 2 *B*). Regions were chosen for doublet normalization in an attempt to average out some of this variability by including inner and outer walls and protofilaments, but dynein arm intensity still varied considerably from one sample to the next. We noticed, however, that the intensities of the outer and inner arms varied together, as they do in these examples. We therefore adopted a second normalization procedure based on the outer arm. With normalization on the outer arm, the inner arms in the three samples appear similar in shape and intensity (Fig. 2, *D–F*). Fig. 2 also shows three samples of the *pf9-2* strain (Fig. 2, *G–I*). Each sample was processed in parallel with the wild-type sample to the left of it. In these outer arm–normalized images, the inner arms from the mutant samples appear reasonably similar to one another and different from the

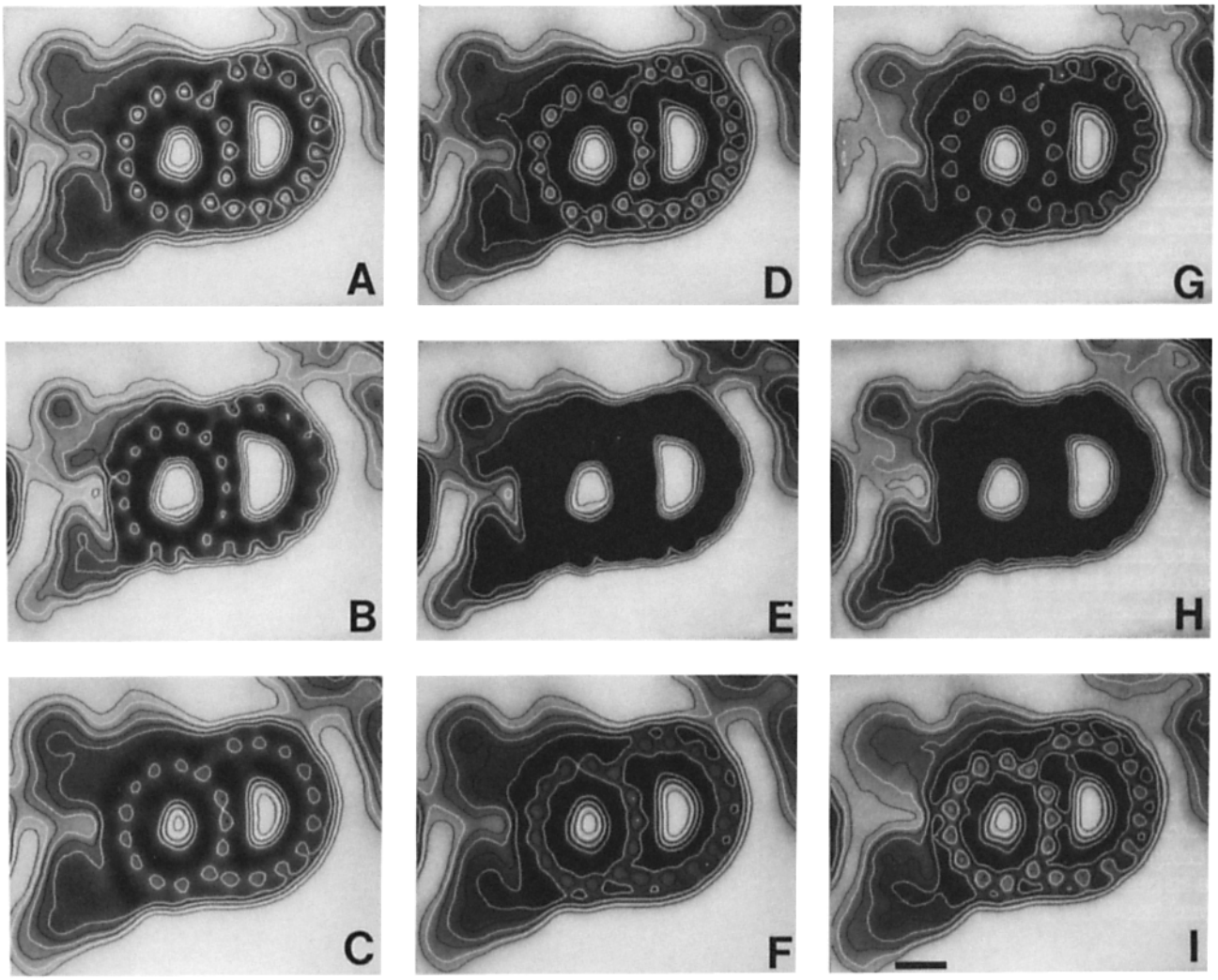

Figure 2. Averages from samples processed in three independent preparations with two different kinds of intensity normalization. (*A–C*) Averages with wild-type inner arms, normalized on the outer double microtubules. The levels of the contour lines are the same in these three examples. Averages of 111, 99, and 127 doublets, respectively. (*D–F*) The same three averages, normalized on outer arms, have more comparable inner arm intensities. The levels of the contour lines are the same as in all of the other outer arm–normalized averages in later figures. (*G–I*) Averages from three independent *pf9* samples processed in parallel with the wild-type samples in *D–F*, respectively. Note the similarity in staining of the microtubule and outer arm structures between samples processed together. Averages of 42, 60, and 73 doublets, respectively. The strains used for *F* and *I* are actually $sup_{pf}1$ and $sup_{pf}1$ *pf9-2* recombinants, respectively, which contain a small deletion (~1 kD) in the β outer arm polypeptide (Huang et al., 1982). We have included these two samples as wild-type and *pf9* because the biochemical deficiency is such a small fraction of the total outer arm mass, and because averages showed no apparent defect in outer arm structure. Bar = 10 nm.

wild-type arms. Moreover, samples processed together show remarkably similar doublets and outer arms.

A quantitative analysis supports these impressions and shows that although dynein arms and doublet microtubules stain variably and independently of each other, the inner and outer arms stain proportionally. To compare images, we have used image integrals, which are the product of the mean intensity and the number of pixels within any given region. Such integrals should be roughly proportional to staining intensity because our normalization procedure scales the mean intensity of the background to near zero. In Fig. 3 *A*, the integral of the outer arm in doublet-normalized images is plotted by day of fixation. Outer arm intensity varies between samples but variability is greater between samples fixed on different days. The range of integrals for samples processed together is typically about one-third as big as the total range of integrals in Fig. 3 *A*. Fig. 3 *B* shows inner versus outer arm integrals from doublet-normalized images, and least-squares lines fit to the points, for samples with a wild-type phenotype and samples with a phenotype characteristic of *pf9*. Variation in outer arm intensity accounted for 92 and 84% of the variance in the inner arm integrals for wild-type and mutant samples, respectively. Moreover, the inner and outer arm intensities were directly proportional to each other, since the intercepts of the lines are not significantly different from zero (intercept $\pm$ standard error = 15 ± 49 for wild type and -1 ± 55 for *pf9*). Normalization on outer arm intensities can thus provide a much better basis for quantitative comparison of inner arms between samples.

The other key to quantitative comparison between strains

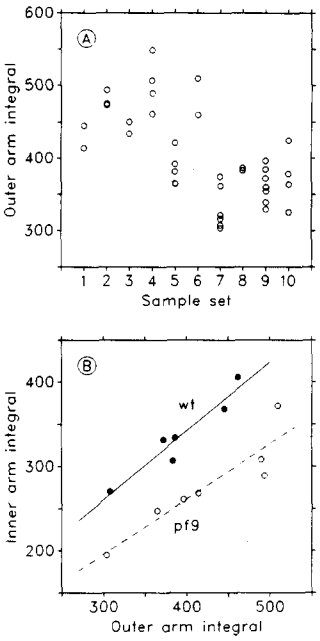

Figure 3. Variation in staining intensity with day of fixation, and covariation in staining of inner and outer dynein arms. Image intensities were normalized on the outer doublet microtubules, and integrals were computed from the product of mean intensity and number of pixels in the inner or outer arm regions. For reference, the average outer arm integral of samples without outer arms was 40 intensity units. (*A*) Integrals from all outer arm containing samples that were processed on each day; integrals did not vary consistently depending on strain. (*B*) Inner arm integral plotted vs. outer arm integral, and separate regression lines, for samples with wild-type phenotype (wild-type and R11 revertants) and for *pf9-1* and *pf9-2* samples.

is the inclusion of multiple samples of each type. As shown in Fig. 2, even with outer arm normalization there are apparent differences in the shape and intensity of the dynein arms between samples of the same strain. In fact, such differences are generally statistically significant, meaning that if the averages were based on many more doublets, the differences would still appear. So as not to be misled by the characteristics of a particular sample, it is necessary to average different samples that encompass the range of intersample variability. We have thus based our statistical comparisons between strains on at least three separate samples of each type.

Comparisons of Wild-Type and pf9 Strains

We have used multiple-sample averages to compare the structural phenotype of wild-type inner arms with those of two different mutations at the *PF9* locus and with that of an intragenic revertant of the *pf9-2* mutation. An average image based on three wild-type samples appears in Fig. 4 *A*. In cross-section, the inner dynein arm has a peak of density in its main, inward-directed portion, and an outward-directed side projection of density. We refer to these two regions as the inner and outer domains, respectively. The most obvious structural defect in the average from *pf9-2* samples (Fig. 4 *D*) is a major loss of density in the outer domain. However, the inner domain is also weaker than in wild-type samples; note the difference in contour levels between mutant and wild-type images.

Quantitative comparisons of integrated intensities in different regions of the inner arm confirm that although the major defect in *pf9* images is in the outer domain, significant differences do exist elsewhere. Fig. 5 shows outer arm–normalized integrals expressed on a relative scale for the whole inner arm, outer and inner domains, and the base of the arm (regions "IA", "OD", "ID", and "B" in Fig. 1 *E*). Each value plotted is the mean of integrals from several samples, with error bars showing 74% confidence limits. Both the inner domain and the base regions of *pf9-2* have highly significant reductions in intensity relative to wild type.

A comparison of two mutations at the *PF9* locus shows that the structural defect is not allele specific. The average image from three samples of *pf9-1* axonemes in Fig. 4 *E* has very similar inner and outer arms to the *pf9-2* average in Fig. 4 *D*, consistent with the similarity in the observed biochemical phenotypes of these two alleles (Porter et al., 1992). The integrated intensities of the inner arm and its subregions do not differ significantly between the strains (filled triangles in Fig. 5). Fig. 4 *F* shows the difference between the average images, where differences that are not significant at the 95% confidence level have been set to zero, based on a pixel-by-pixel nested analysis of variance (see Materials and Methods). This image makes it clear that whatever subtle differences do appear between the dynein arms of the two allelic strains, they cannot be confidently attributed to anything besides intersample variability. Note that the apparently substantial differences between doublets in Fig. 4, *D* and *E* do not show up in the difference plot. These regions have sufficient variability among the samples of each strain so that the differences between strains are not statistically significant.

Our analysis of the intragenic revertant R11 of the *pf9-2* mutation shows that its structural phenotype is wild-type, consistent with its biochemical phenotype (Porter et al., 1992). The inner arm in the R11 average image (Fig. 4 *B*) has recovered both the shape and the overall intensity of the wild-type structure (e.g., compare contour lines in Fig. 4, *A* and *B*). The integrated intensities of inner arm regions confirm that there are no significant differences between wild-type and R11 (Fig. 5). The wild-type–R11 difference image (Fig. 4 *C*) does show some features, primarily over the doublet microtubules. However, because two of the three R11 samples were prepared on the same day, we think that these features reflect a failure of the R11 samples to span the full range of intersample variability in staining characteristics, rather than a true difference between wild-type and R11 strains.

To obtain the best possible estimate of the location and extent of the structural defect in the inner dynein arm of the *pf9* strains, we pooled images from the *pf9-1* and *pf9-2* samples (Fig. 4 *H*) and images from the wild-type and R11 samples (Fig. 4 *G*). Both the difference image (Fig. 4 *I*) and the pooled integrated intensities (Fig. 5) show that the greatest defect in the *pf9* samples is localized on the outer domain of the inner arm, but significant deficiencies are observed throughout the inner arm. The reductions in intensity from wild-type to mutant samples are 24% for the whole inner arm, 35% in the outer domain, 22% in the inner domain, and 15% in the base of the inner arm. Since *pf9* axonemes are missing the polypeptides associated with the I1 subunit of the inner arm (Fig. 1 of Porter et al., 1992), this difference image provides a projected, cross-sectional view of the structure associated with the I1 subunit. Again, this structure is not located entirely in the outer domain, nor is it the only constituent of the outer domain.

Analysis of Other Inner Arm Mutations

Our success with the *pf9*-related strains led us to examine the structural phenotypes of two other mutant strains that have been reported previously to alter inner arm polypeptides, *pf23* and *pf2*. Axonemes from *pf23* strains have previ-

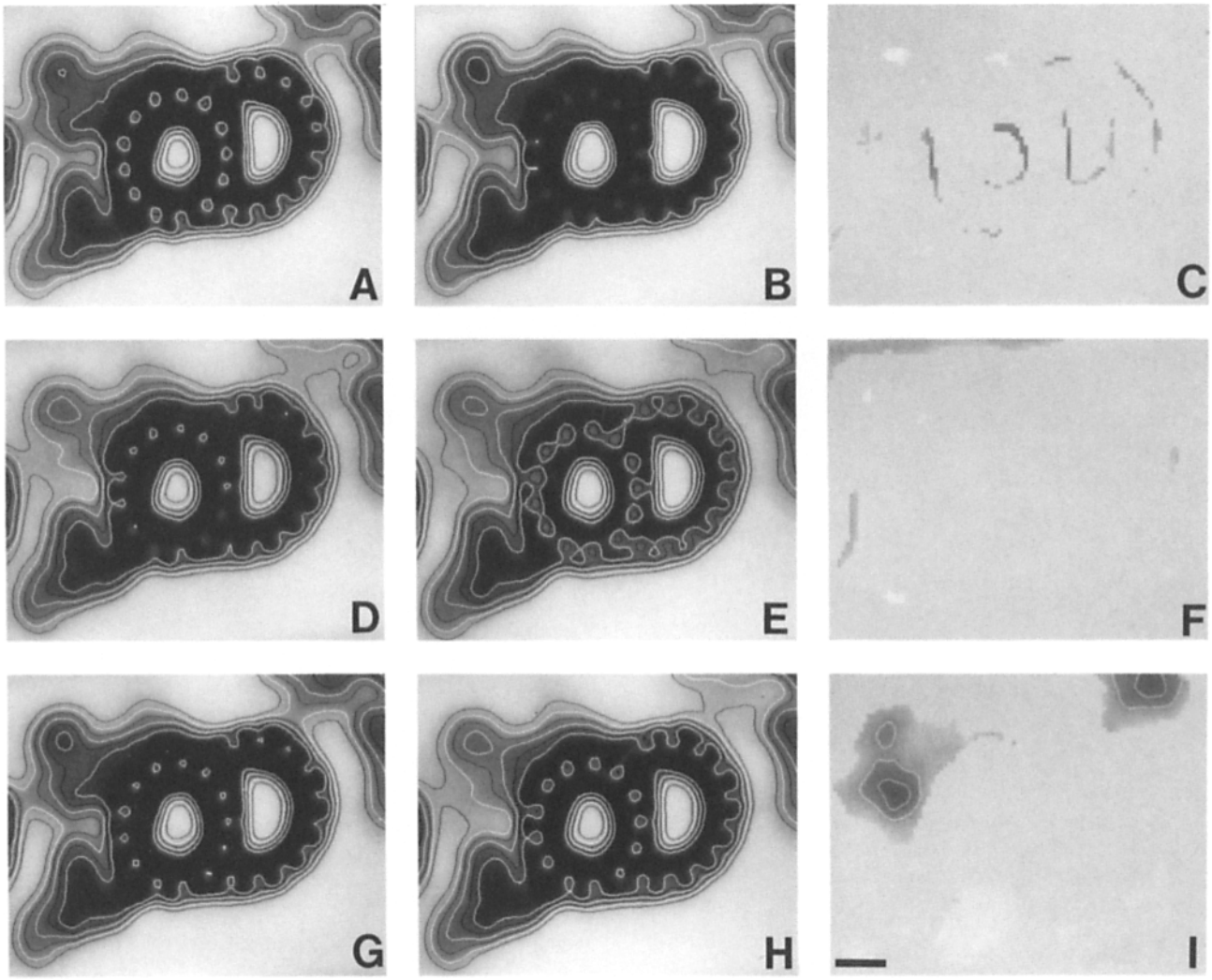

Figure 4. Average images and "significant difference" images for samples with wild-type and *pf9* phenotypes. (*A*) Grand average of three wild-type samples, involving a total of 337 doublets. (*B*) Grand average of three R11 samples containing 215 doublets. (*C*) Subtraction of R11 from wild type, with differences not significant at the 0.05 level set to zero. The interval between contour lines in this and other difference images is the same as in the average images, 0.15 intensity units. (*D, E*) Averages of four *pf9-2* and three *pf9-1* samples containing 235 and 257 doublets, respectively. (*F*) Subtraction of *pf9-1* from *pf9-2*. (*G, H*) Averages of all samples with wild-type phenotype (wild-type and R11) and of all *pf9* samples; (*I*) difference between the two. Bar = 10 nm.

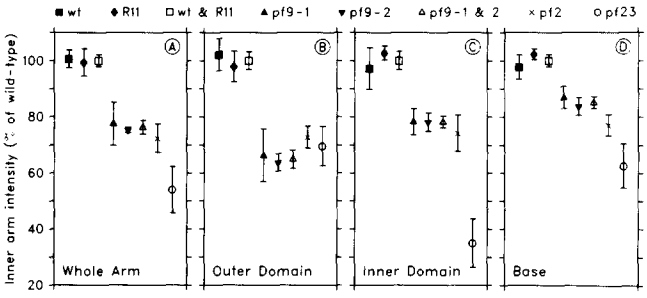

Figure 5. Integrated intensities of the whole inner arm and three subregions for the strains analyzed in this study. For each region, the integrals are expressed as percentages of the mean integral for samples with wild-type phenotype (wild-type and R11). Each point shows the mean over all of the samples for the particular strain; error bars are 74% confidence limits. With these confidence limits, error bars typically would not overlap for means that are significantly different at the 0.05 level with a one-tailed *t* test. Regions are defined in Fig. 1 *E*.

ously been described as nearly completely deficient in inner arm structure, based on cross-sectional images (Huang et al., 1979), or deficient in two of three inner arm subspecies, based on longitudinal images (Piperno et al., 1990). Our analysis of *pf23* in cross-section shows a distinct phenotype, with density missing from both the inner and outer domains of the inner arm (Fig. 6 *A*). Subtraction from the wild-type average shows that *pf23* has a strong reduction in intensity in the inner domain of the inner arm and a weaker loss in the outer domain (Fig. 6 *B*). The latter is in about the same position as the main loss in *pf9*. These results are consistent with the observation that *pf9* and *pf23* share a common deficiency in the 1α/1β polypeptides of the I1 inner arm subunit (Fig. 3 of Porter et al., 1992). The overall loss of intensity of the inner arm in *pf23* is 46%, about twice the loss in *pf9* (Fig. 5). The appearance of the average is misleading in suggesting an almost complete loss of inner arm density. Examination of doublets in individual cross-sections reveals that the average includes a wide diversity of structures, rang-

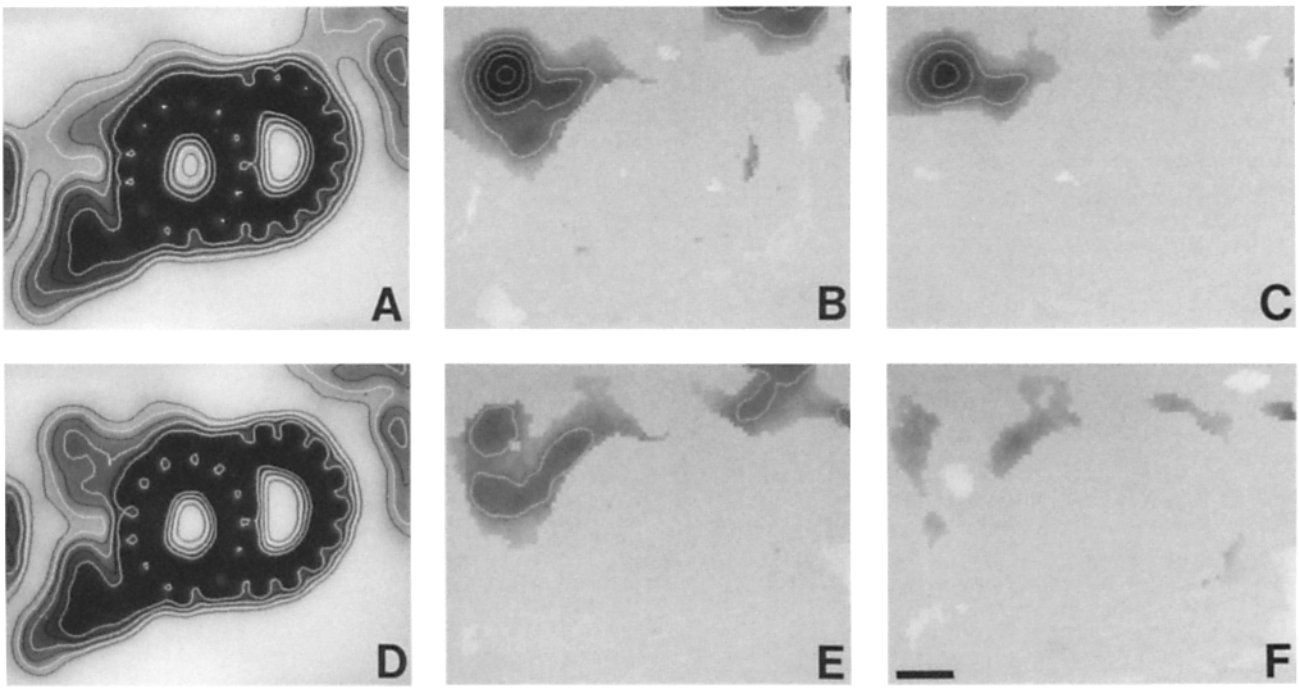

Figure 6. (*A*) Average of five samples from *pf23* containing 379 doublets. (*B, C*) Subtraction of *pf23* average from averages of all samples with wild-type and *pf9* phenotypes, respectively. (*D*) Average of four samples from *pf2* containing 331 doublets. (*E, F*) Subtraction of *pf2* from wild-type and *pf9*, respectively. Bar = 10 nm.

ing from virtually no inner arm to a rather robust inner arm, with the majority of doublets having detectable inner arm material. This diversity presumably reflects two factors: the variable placement of the 60-nm cross-section within the 96-nm repeating unit of the axoneme, and the fact that the inner arm material remaining in *pf23* is confined to a portion of the repeating unit (see below and Piperno et al., 1990). In any case, the density remaining in *pf23* is difficult to discern in the average image because it is not much above background. In fact, the inner arm density outside the lowest contour line is about as strong as the radial spoke density (Fig. 6 *A*). Thus, even the inner domain is not lost entirely and retains 35% of the wild-type intensity (Fig. 5 *C*; note that the scale in Fig. 5 does not extend to 0). The extent and location of the remaining density are more readily apparent in the longitudinal averages presented below.

It is also illuminating to compare the structural deficiencies of *pf9* and *pf23* directly. By subtracting the *pf23* from the *pf9* average, we see that the extra loss in *pf23* is located predominantly in the inner domain and also in the base of the inner arm (Fig. 6 *C*). Since *pf23* is missing the 2, 2′, and 3′ heavy chains in addition to the 1α/1β subunit (Piperno et al., 1990; Porter et al., 1992), this difference image provides a projected, cross-sectional view of the structure associated with at least some of these additional polypeptides. Although this structure contributes primarily to the inner rather than the outer domain, both the inner domain loss in *pf9* and the remaining inner domain density in *pf23* clearly show that these polypeptides are not the only constituent of the inner domain. Thus, other polypeptide components remain in both domains of the inner arm region in *pf23*.

The *pf2* mutant strain has an abnormal motility phenotype similar to that described for other inner arm mutations (Brokaw and Kamiya, 1987). Previous studies have indicated that *pf2* axonemes are missing four axonemal polypeptides associated with the radial spoke suppressor control system (Huang et al., 1982), but the location of these polypeptides in the axoneme has not been determined. Others have reported that the *pf2* strain shows defects in the phosphorylation of inner arm heavy chains (Luck and Piperno, 1989). Our analysis of this mutant strain illustrates the power of our methods for revealing subtle differences between strains. The average image for *pf2* shows a loss of inner arm intensity relative to wild-type (compare Fig. 6 *D* with Fig. 4 *G*); the total loss in intensity is about the same as that observed in *pf9* samples (Fig. 5 *A*). However, the overall appearance of the inner arm retains the same basic shapes as in the wild-type (see contour lines), and the difference between wild-type and *pf2* averages shows that the intensity loss is evenly distributed throughout the inner and outer domain and base regions (Fig. 6 *E*). Indeed, the intensity losses in these regions are 26, 27, and 23%, respectively. Compared with *pf9*, the *pf2* average has significantly more intensity in the outer domain and significantly less in the base and in the tip of the inner domain (Figs. 5 and 6 *F*). These results indicate that the polypeptides deficient in the *pf2* strain are located in different positions than those deficient in *pf9*, in agreement with our biochemical data (Fig. 3 of Porter et al., 1992).

Analysis of Serial 24-nm Cross-Sections

The cross-sectional averages show density missing from different inner arm domains in various mutant strains, but because of the relatively thick sections used, these averages provide no information on the distribution of the missing density within the 96-nm repeating unit of the axoneme. There are thus alternative interpretations of these data: den-

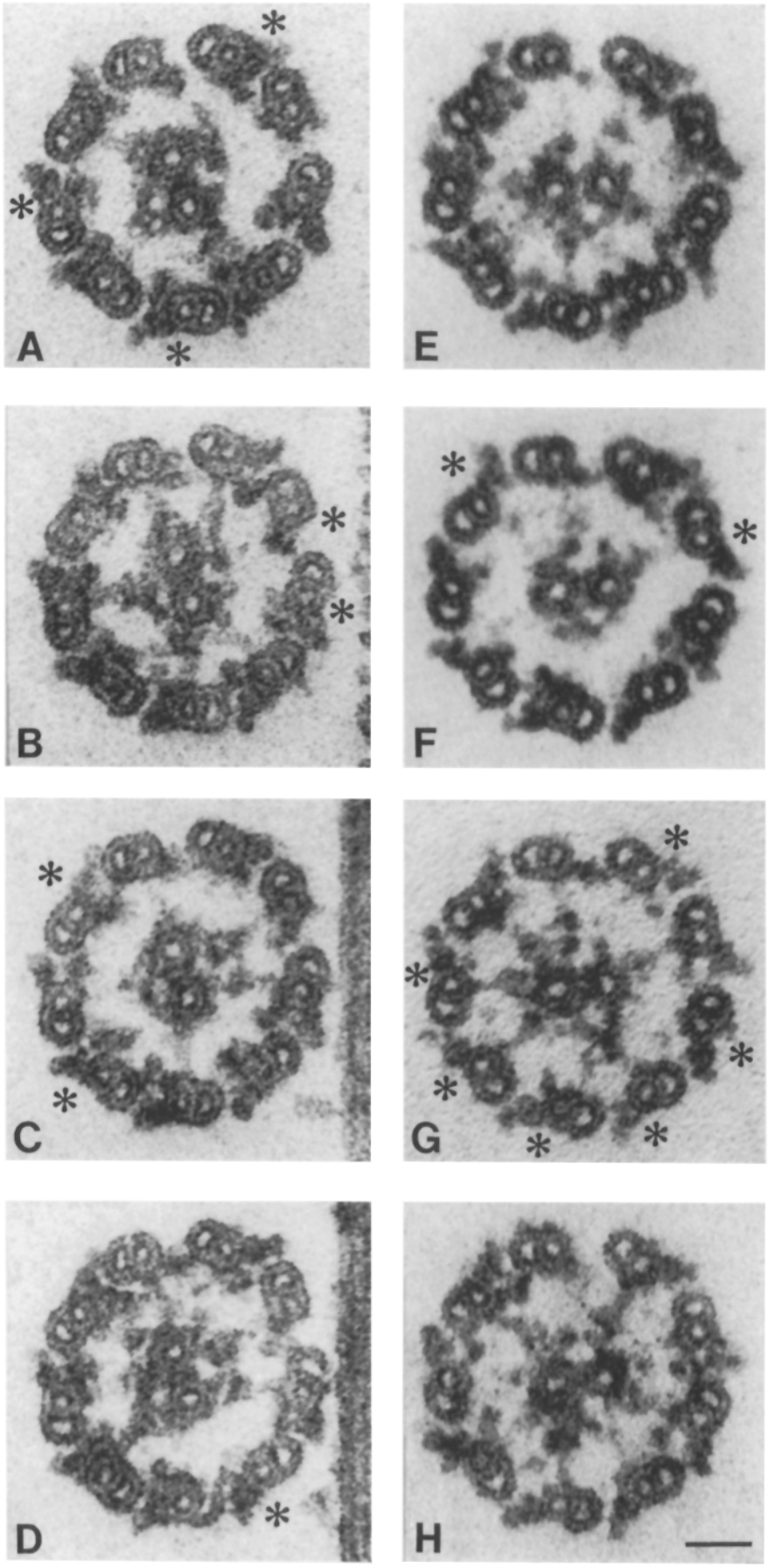

Figure 7. Four serial 24-nm cross-sections spanning one 96-nm repeating unit, for wild-type (*A-D*) and *pf9* (*E-H*). Images are arranged to display sections from proximal to distal along the flagellum. For each outer doublet except the one missing an outer arm (doublet 1), the asterisk marks the section at the proximal end of the repeating unit, based on an examination of radial spoke density, as described in the text. The images have been aligned to each other and adjusted to have the same mean and variance of intensity. Bar = 50 nm.

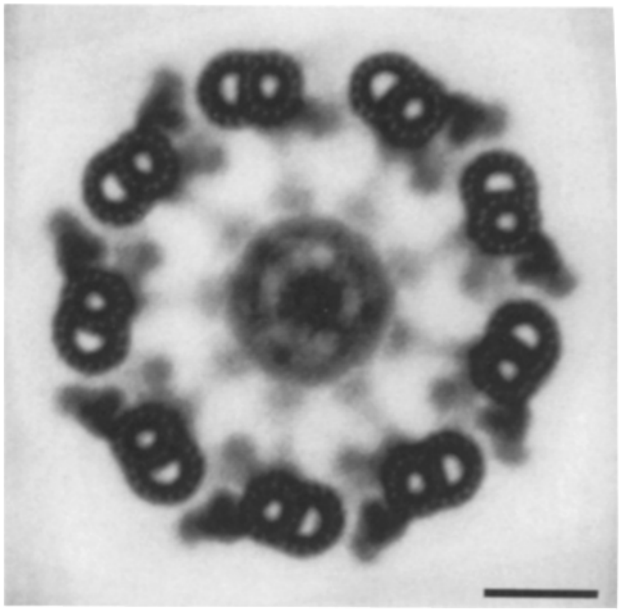

Figure 8. Average of seven different *pf9* axonemes, each averaged over 13 serial 24-nm sections. The *pf9* structural deficiency is present on every doublet, with the possible exception of doublet 1. The 13 sections were aligned and averaged for each axoneme, then the seven averages were aligned and averaged. Bar = 50 nm.

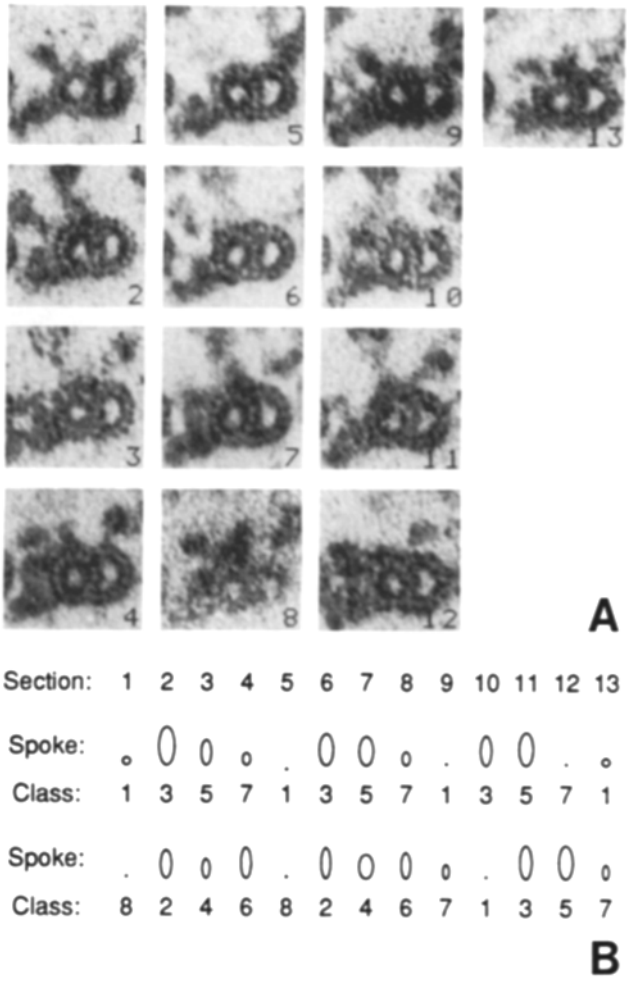

Figure 9. (*A*) Example of images from one outer doublet in the 13 serial 24-nm sections. Each column contains one repeating unit. Each image is 81 nm square. (*B*) Examples of the drawings used to analyze the positions of the radial spokes within the serial sections for each doublet. See text for details. The upper drawing corresponds to the example in *A*.

sity could be missing from a discrete location within the repeating unit, as proposed by Piperno et al. (1990), or it could be lost all along the length, such as from one of two parallel rows of projections, as suggested by Kamiya et al. (1991). We have used two methods to obtain three-dimensional information on inner dynein arm structure: an analysis of serial cross-sections with a nominal thickness of 24 nm, and averaging of images from longitudinal sections. We present the results from the former method first because they can be related directly to the standard cross-sectional averages shown above.

Our examination of serial 24-nm sections confirms that the polypeptides missing from *pf9* axonemes normally reside at discrete locations within the repeating unit. To maximize contrast in the electron micrographs of these very thin sections, we studied our most heavily stained samples (the wild-type and *pf9* samples whose averages appear in Fig. 2, *F* and *I*). We analyzed two wild-type axonemes from one set of 12 serial sections and seven *pf9* axonemes, all from one set of 13 sections. For each digitized axoneme, the serial images were first brought into common alignment by general linear transformations, using the centers of the doublet microtubules as fiducial points. Examples of four serial sections, spanning one 96-nm repeating unit, are shown in Fig. 7, *A–D* for a wild-type axoneme and in Fig. 7, *E–H* for a *pf9* axoneme. Numerous doublets in the *pf9* axoneme have completely missing or very weak inner arms, while virtually all doublets in the wild-type sections have inner arms. Moreover, *pf9* doublets are not missing arms along their entire length but only in one or two of the four serial sections. Note that it is not reasonable to expect every doublet to show a complete absence of structure unless the gap in structure is at least twice the section thickness; with a gap narrower than this, whenever the cut between two sections falls near the middle of the gap, both sections will show material from either side of the gap.

The impression from examining sections such as those in Fig. 7, *E* and *F* is that gaps could be observed on any of the *pf9* doublets, with the possible exception of doublet 1, the one missing the outer arm (Hoops and Witman, 1983). To determine whether it was valid to include all doublets in the analysis, we averaged the aligned images of each *pf9* axoneme over the 13 serial sections. We then brought the average images of the seven axonemes into common alignment to obtain the average shown in Fig. 8. The inner dynein arm on doublet 1 appeared different, so we omitted this doublet from all further analysis. The rest of the doublets, however, had the characteristic *pf9* morphology. Quantitative analysis of each doublet position did reveal some subtle differences among the other positions, but each doublet's inner arm structure was within the range found for cross-sectional averages of *pf9* samples and well outside the range seen for wild-type samples. This result demonstrates that the *pf9* polypeptide deficiency is present at all eight of the doublet positions that we analyzed.

To relate the position of missing inner arms to the 96-nm repeating unit, we examined the pattern of radial spokes for each doublet through the series of sections. As an example, Fig. 9 *A* shows the 13 serial images of one doublet from a *pf9* axoneme, arranged from proximal to distal. Note that the pattern of spokes repeats every four sections, with spokes present only in the middle two rows of sections. This repeating pattern indicates that the average thickness of these sections was quite close to one-quarter of the length of the axonemal repeating unit. To aid in the detection of such patterns, we examined each doublet in each section and drew an ellipse whose area was roughly proportional to the amount of spoke material judged to be associated with that doublet, based on the product of the perceived size and density of the spoke material. Fig. 9 *B* is based on these drawings for two doublets from one *pf9* axoneme. The upper set of drawings, derived from the doublet in Fig. 9 *A*, shows one common pattern in which spokes are strong in two adjacent sections and then weak or absent in the next two. The other common pattern is shown at the left side of the lower drawings, where spokes appear in three successive sections and are then absent in one section. Here, the pattern shifts from one form to the other after section 8, which was an exceptionally thin section (note the poor image for section 8 in Fig. 9 *A*). Such shifts occurred often. Sometimes the middle section of three had a much weaker spoke than the other two (e.g., lower left spokes in Fig. 9 *B*), indicating that that section fell predominantly on the gap between the two spokes. Based on these patterns, we assigned images of individual doublets to eight classes: 1, 3, 5, and 7 when spokes appeared in only two adjacent sections, or 2, 4, 6, and 8 when spokes were spread over three sections (see class assignments in Fig. 9).

The doublets at the beginning of the repeating unit (class 1 or 2) are marked with stars in Fig. 7. In the *pf9* axoneme, the inner arms are weak or absent in the marked positions; for half of these doublets, the inner arm is also weak in one of the two adjacent sections. Thus, although the synchronization between inner arms and spokes is not perfect, the inner arm is missing from the most proximal portion of the repeat unit, as is seen in longitudinal sections (see below).

We averaged the doublet images in each of the classes defined by spoke morphology and found progressive changes in the appearance of the inner dynein arm through the 96-nm repeat. The averaging procedure differed from the standard method in two respects. First, virtually all individual doublets were included except ones from position 1 and ones from the very thin section. Second, because the serial section alignment rendered all of the axoneme cross-sections circular and similar in size, only rotations and translations were needed to align all of the individual doublets for averaging. Despite these differences, and the use of much thinner sections, the average of all 677 doublets from the thin serial sections (Fig. 10 *A*) closely resembles the standard cross-sectional average from 60-nm sections of this sample (Fig. 2 *I*), especially in the appearance of the dynein arms.

Fig. 10 *B* shows the average structure of the inner arm at each position of the 96-nm repeat. The weakest inner arms appear in the most proximal classes, 1 and 2, which reflects the gap observed in individual sections. The inner arm image in each class should be considered to be contaminated by those in the two adjacent classes for three reasons: first, the section thickness is twice the interval between classes; second, assigning doublets to classes is an inherently inaccurate process; and finally, the inner arms may not be perfectly synchronized to the spoke pattern used to classify doublets. Thus, class 1 shows a ghost of the distal structures that predominate in class 8, whereas class 2 shows a ghost of the proximal structures distal to the gap, which predominate in class 3. Classes 3 and 4 show a simple projection in the inner

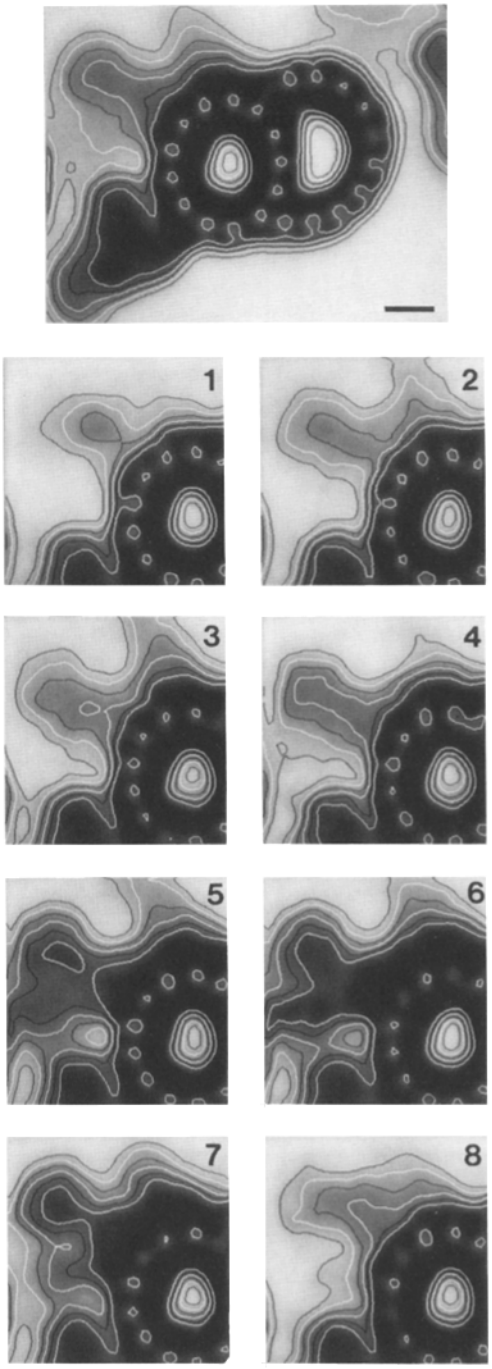

Figure 10. Cross-sectional averages at a series of eight positions within the 96-nm repeating unit. (*A*) Grand average of 677 doublet images from all eight positions. (*B*, *1–8*) Averages from the doublets in the eight positions or classes, containing 100, 66, 102, 61, 114, 65, 96, and 73 doublets, respectively. These averages were low-pass filtered to a resolution of 4.5 nm, then renormalized on outer doublet microtubules. Bar = 10 nm.

domain, similar to the structure seen in the difference between *pf9* and *pf23* averages (Fig. 6 *C*). In classes 5–7, the inner arm stains more intensely and appears more complex, with significant structure in the outer domain. The latter includes a possible linkage between adjacent doublets; note the density that appears attached to the B subfiber of the adjacent doublet in class 5, becomes an extended structure in class 6, and ends as a short stub between the inner and outer arms in class 7. Finally, in the most distal class, 8, the inner arm is located more inwardly and has a distinctive hook shape.

In contrast to the outer arms, which appear the same throughout the repeating unit, the inner arm region shows complex shifts in structure through the repeating unit and may contain elements other than dynein arms. The series of averages suggests the following interpretations. First, the shifts in structure as one moves through the 96-nm unit are not consistent with a simple repeat of two similar inner arms. For example, the hook-shaped arm in class 8 is more inwardly located than the inner arm in any of the more proximal classes. Also, from classes 4–8 there is a slight inward shift in the point of apparent attachment of the dynein arm to the doublet microtubule. Second, not only does the *pf9* strain clearly retain some density in the outer domain, but these outer structures are also concentrated in one portion of the repeating unit. Third, the inner arm region may not contain just dynein arms; the apparent link between adjacent doublets in classes 5–7, described above, may be the nexin or interdoublet link (Warner, 1983). Finally, when a point of attachment appears in a standard thin section or average image, it is tempting to assume that it occurs throughout the length of the repeating unit, but such an attachment may be quite localized within the repeating unit. This point applies to the apparent link between doublets. Similarly, a structure located between the main inner arm and the radial spoke has been suggested to be a point of attachment for the inner arm (Kamiya et al., 1991), but the averages in Fig. 10 *B* reveal that this structure appears only at the distal end of the repeating unit, where the arm appears hook shaped.

Averaging of Longitudinal Sections

Longitudinal views of axonemes have been used extensively to study the structure of the inner dynein arms (Goodenough and Heuser, 1989; Piperno et al., 1990; Muto et al., 1991), but these views can be quite difficult to interpret. To get beyond the limitations inherent in examining individual micrographs, we developed methods for averaging the repeating structure from longitudinal sections. Our averages provide a clearer view of the structures present in the inner arm region along the doublet microtubule and indicate the status of these structures in various mutant strains.

As shown in Fig. 11, progressively more information becomes available as one proceeds from raw micrographs to averages of individual axonemes and then to grand averages for each strain. Fig. 11 *A* shows our best example of a longitudinal section through a *pf9* axoneme; it includes 10 repeats of the basic 96-nm unit. This axoneme and the averages in Fig. 11 are oriented so that the end proximal to the basal body is to the left. The absence of inner arm density just proximal to the radial spokes is clear in this *pf9* axoneme, as was observed in *pf30* (an allele of *pf9*) by Piperno et al. (1990). The average from the lower doublet of this axoneme appears in Fig. 11 *C*. A single repeating unit occupies the central two-thirds of the average and includes four outer arms. This image clearly reveals the average extent of the gap in inner arm material. No such gap appears in averages from wild-type axonemes (e.g., Fig. 11 *B*). A typical average from a *pf23* axoneme (Fig. 11 *D*) appears to be missing more material and to have a larger gap than does *pf9*, also in agreement with Piperno et al. (1990), but it is difficult to say precisely which additional structures are missing.

Additional detail was revealed when we aligned all of the averages with one another (see Materials and Methods) to obtain the grand averages for each strain shown in the lower part of Fig. 11. The inner arm region of the wild-type average (Fig. 11 *E*) shows considerable heterogeneity and is not simply a repeating series of identical structures, consistent with the complexity seen above in the averages from the serial 24-nm sections. By examining this wild-type image together with those for the other strains, we have distinguished 10 structures in the inner arm region; they are drawn schematically and numbered in Fig. 11 *H*. Many of these structures are distinguishable because they contain a separate peak of density. However, some of the boundaries between structures are revealed only by the fact that density is missing in one of the mutant strains. We refer to the structures as lobes because most of them do correspond to separate peaks of density. The various lobes will be described in the context of particular mutant strains.

Comparison between the grand averages of wild-type (Fig. 11 *E*) and *pf9* (Fig. 11 *F*) indicates that the density missing in *pf9* occupies a boot-shaped region containing three distinguishable lobes: a closely associated pair at the proximal end of the repeating unit (lobes labeled 1 and 2 in the schematic drawing of Fig. 11 *H*), and a somewhat separated, elongated

Figure 11. Analysis of longitudinal sections of wild-type and mutant axonemes. (*A*) 10 repeating units from a *pf9* axoneme. Bar = 50 nm. (*B–D*) Averages from individual wild-type, *pf9*, and *pf23* axonemes, based on 5, 10, and 5 repeating units, respectively. (*E–G*) Grand averages for wild-type, *pf9*, and *pf23*, based on 9, 6, and 11 individual axonemes, involving a total of 62, 30, and 71 repeats, respectively. These and other grand averages do not include: (*a*) averages from two very heavily stained samples (the ones used in the analysis of 24-nm sections); (*b*) atypical averages, nearly all of which were from *pf23*; and (*c*) a few other averages that failed to resolve structures in the inner row or that appeared to have particularly truncated outer arms. The grand average for *pf9* (*F*) is based on only one of two samples that were examined. The average from both samples (involving 11 axonemes and 80 repeats) was used to prepare the difference images shown here. (*H*) Schematic diagram of the distinguishable densities present in these averages. S1 and S2 are radial spokes 1 and 2. (*I, J*) Differences between wild-type and *pf9* or *pf23*, respectively. Difference images were computed by performing a *t* test at each pixel, based only on the variance among the individual averages of each strain and ignoring variability within each average. Differences not significant at the 0.005 level were set to zero. (*K*) Grand average from five *ida4* axonemes containing a total of 44 repeats. The difference from wild-type (*L*) shows the same structures as the difference between *pf9* and *pf23* (*M*). (*N*) Grand average from 13 *pf2* axonemes containing a total of 98 repeats. (*O, P*) Differences between wild-type or *pf9* and *pf2*. Bar = 25 nm in *B–P*.

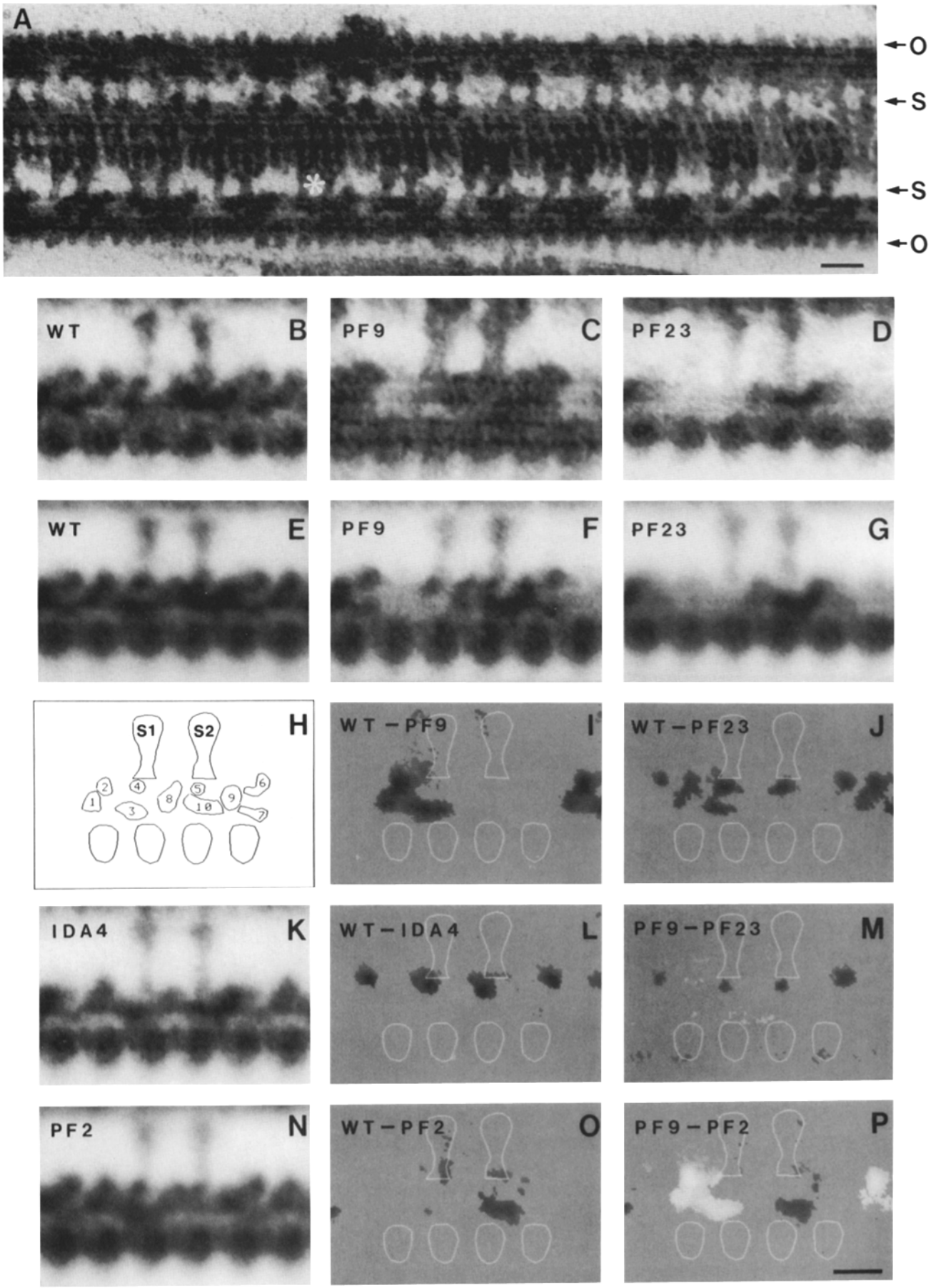
A
O
S
S
O
WT
B
PF9
C
PF23
D
WT
E
PF9
F
PF23
G
S1
S2
H
WT – PF9
I
WT – PF23
J
IDA4
K
WT – IDA4
L
PF9 – PF23
M
PF2
N
WT – PF2
O
PF9 – PF2
P

lobe (labeled 3) that lies below radial spoke 1 (S1). To make this and other comparisons quantitatively, image intensities were normalized by a method similar to that used for the cross-sectional averages. The mean intensity of two regions without structure, one to the left of S1 and one to the right of spoke 2 (S2), was set to zero, and that of a long, narrow rectangle spanning the densest part of the outer dynein arms was set to 1.0. Outer arm normalization was not as successful at equalizing intensities here as for the cross-sectional averages, perhaps because outer arms were truncated by small but variable amounts in the various longitudinal sections, or because the outer arms were not well aligned between the various averages, or because grand averages were based on only one or two samples of each strain. The significant difference images here are thus less sensitive than those from cross-sectional averages and a more stringent significance level, 0.005, was needed to obtain images with a comparable signal-to-noise ratio. The wild-type–*pf9* difference image of Fig. 11 *I* isolates the three lobes described above and shows no other consistently significant differences, thus supporting the visual impression that other structures in *pf9* appear to be wild-type. The structures appearing in this difference image thus represent the I1 subunit that is missing in *pf9* axonemes.

When compared with wild-type and *pf9* averages, the *pf23* average (Fig. 11 *G*) is missing the I1 subunit and also structures in three separate locations: two small lobes (labeled 4 and 5) below the ends of the radial spokes, and a larger, inwardly placed lobe (labeled 6) at the distal end of the repeating unit. These three lobes appear together with the I1 subunit in the difference between *pf23* and wild-type (Fig. 11 *J*) and they appear alone in the difference between *pf23* and *pf9* (Fig. 11 *M*). The elongated, outwardly placed lobe (labeled 7) at the distal end of the repeating unit also appears to be reduced or absent in *pf23*, but this loss does not show up as significant in either of those two difference images (see below).

There was more variability among the averages for *pf23* than for any other strain, primarily because some images retained the I1 subunit. Two averages had clear I1 structures and two others showed them faintly; these four axonemes were all from one of the three samples of *pf23* that we examined. Even the axonemes included in the grand average of Fig. 11 *G* seem to have had some residual I1 structure, which is why the image of I1 is weaker in the wild-type–*pf23* difference than in the wild-type–*pf9* difference.

The structures present in *pf9* but absent in *pf23* have been proposed to constitute the I2 subspecies, composed of inner dynein heavy chains 2 and 2′ (Piperno et al., 1990). To determine whether the additional loss in *pf23* is indeed simply the I2 subspecies, we examined the axonemes from the *ida4* strain, which is deficient in 2 and 2′ but not in the 1α and 1β heavy chains (Kamiya et al., 1991). Comparison of *ida4* (Fig. 11 *K*) with wild-type shows that the I1 subunit is present, but that the other structures deficient in *pf23* are missing in *ida4*. Lobes 4–6 are clearly missing from noncontiguous locations and, just as in *pf23*, the thin distal lobe (7) appears reduced or abolished, but this apparent deficiency is not significant enough to show up in the difference between wild-type and *ida4* (Fig. 11 *L*). The wild-type–*ida4* and *pf9*–*pf23* differences show the same three lobes (Fig. 11, *L* and *M*), illustrating graphically that the additional deficiency in *pf23* is the same as that in *ida4*. These three lobes, and possibly lobe 7, are thus components of the I2 subspecies. Lobes 4 and 5 are comparable in size and in their locations relative to the spokes; they may well be identical subunits. However, all three of the relevant difference images (Fig. 11, *J*, *L*, and *M*) indicate that the distal-most lobe (6) is located more inwardly than the two below the spokes. This lobe should correspond to the hook-shaped, inwardly placed inner arm seen at the distal end of the repeating unit in the averages from serial 24-nm sections (Fig. 10 *B*, *8*). Both methods of analysis thus indicate that this lobe is unlikely to be identical to the other I2 subunits.

We also obtained longitudinal averages from the *pf2* strain because its cross-sectional average showed a deficiency distinct from that of the other strains examined. The results allow a subdivision of the inner arm structures remaining in *pf23* (Fig. 11 *G*). These unassigned structures consist of a light density proximal to S2 (the lobe labeled 8, which a few of the grand averages suggest consists of two portions), and a heavily staining, crescent-shaped density below and distal to S2 (labeled 9 and 10). The latter appears to be a single structure in the other grand averages, but the average from *pf2* (Fig. 11 *N*) shows a clear deficiency in the proximal part of the crescent (lobe 10). Thus, this is the probable location of the polypeptides missing in *pf2*, which have been postulated to comprise a "spoke control system" (Huang et al., 1982). This is the only consistent deficiency that shows up as significant in the differences between *pf2* and wild-type or *pf9* (Fig. 11, *O* and *P*). However, lobe 5, under S2, also appears reduced in intensity in the average. This lobe was weak or absent in one-third of the averages from individual axonemes. A deficiency at this position is consistent with our data from cross-sectional averages. Since the major deficiency, lobe 10, would contribute mostly to the outer domain in cross-sectional averages, there must be some additional, inward-directed deficiency, such as lobe 5, to account for the nearly equal loss in inner and outer domains in *pf2* averages.

Because of uncertainty about the status of the outer lobe at the distal end of the repeating unit (lobe 7), we examined this lobe in the averages from individual axonemes. There was more variation in presence or absence for this lobe than for any other lobe. For each average, we characterized the lobe as present, weak, absent, small, or displaced from its typical position. For three strains, the lobe was usually present (8–9 of 10 wild type, 9 of 11 *pf9*, 8 of 12 *pf2*); for the strains deficient in I2 polypeptides, it was seldom present (0–1 of 5 *ida4*, 2–4 of 11 *pf23*, where the upper values of each range include small or displaced lobes). Although the variability for this lobe is puzzling, these counts suggest that it is a component of the I2 subspecies.

Discussion

We have taken three approaches to determine the three-dimensional arrangement of the inner dynein arms in wild-type, mutant, and revertant axonemes of *Chlamydomonas*. We developed methods for averaging cross-sectional images in order to localize the deficiencies in mutant strains and make relatively sensitive comparisons between different strains. We analyzed ultra-thin serial cross-sections to obtain information on the variation in structure through the length of the 96-nm repeating unit, thus obtaining results that

could be related directly to the overall cross-sectional view of the structure. Finally, we averaged images from longitudinal sections and obtained a clear picture of the structures present in the inner row of dynein arms. We determined which structures were missing in particular mutant strains, and we thus can provide a significant improvement over several recent models of inner arm structure (Goodenough and Heuser, 1989; Muto et al., 1991; Piperno and Ramanis, 1991).

Methodological Issues

Our methods for aligning and averaging images were chosen to alleviate some of the distortions inherent in electron microscopy of thin sections. The standard approach for averaging particles (e.g., ones deposited on a specimen support film) is to use image auto- and cross-correlations to find translations and rotations for aligning the particles (e.g., Frank et al., 1978). We noted, however, many individual doublets in our cross-sectional images with noncircular microtubules, even though they had clear protofilaments and were thus in reasonably good cross-section. Image transformations more extensive than translation and rotation were needed to remove these distortions. We thus adjusted for image stretch and changes in magnification as well by using general linear transformations, which have also been used successfully to adjust for distortions and achieve adequate registration between adjacent sections in reconstructions from serially sectioned material (McDonald et al., 1991). Image stretch and magnification adjustments were equally essential for aligning the longitudinal averages from different axonemes with one another. In this case, our ability to adjust the alignment parameters manually was also important.

The main difficulty in our initial analysis of cross-sectional averages was the substantial variability among different samples of the same strain, manifested by variations in the appearance of both the doublet microtubules and the dynein arms, and by the independent staining characteristics of these two structures (e.g., Fig. 2). We have addressed this problem by normalizing intensities on the integral of the outer dynein arm, by processing multiple samples of each strain, and by comparing different strains using statistical methods with a nested structure that explicitly accounted for both intra- and intersample variability. The problem of intersample variability is more severe for strains that lack outer dynein arms because this absence requires that intensities be normalized on the doublet microtubules, a less satisfactory procedure due to the variability in microtubule staining. This difficulty is unfortunate because such strains are much easier to analyze biochemically. When outer arm normalization was possible, we could obtain images of statistically significant differences showing few spurious differences with only three or four independent samples of each strain. We estimate that when the outer arm is missing, one must process two to three times as many samples to obtain comparably clear differences.

Our images are not based on a direct measure of the location of axonemal proteins but rather reflect the deposition of heavy metal stains by unknown mechanisms. The effect of this limitation on our results is hard to assess. Our images should thus be interpreted with some caution, particularly when comparing them with ones prepared with other methods of contrast generation.

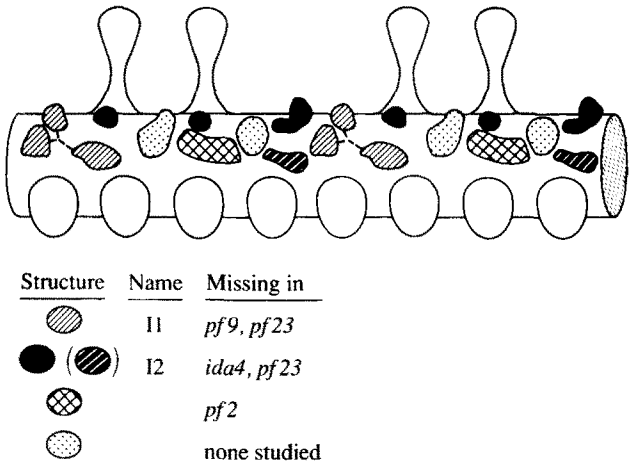

Figure 12. Model of structures attached to the A-subfiber of a flagellar outer doublet microtubule. Outer dynein arms are on the bottom; radial spokes are on the top; two 96-nm repeating units are shown, with the end proximal to the basal body on the left. Structures in the inner row of dynein arms are coded according to the mutant strains in which they were deficient. The lobe marked with thick diagonal lines was weak or absent in most averages from individual *ida4* or *pf23* axonemes, but this deficiency did not achieve statistical significance.

Structure of the Inner Row of Dynein Arms

Fig. 12 presents our model of the structure of the inner row of dynein arms; the shading encodes different classes of structures. In the context of this model, we now discuss issues related to each of the different kinds of inner arm structures.

The I1 subunit, defined as the structure associated with the 1α and 1β heavy chains, consists of three lobes of density. Two of these are located near the outer arms, but the other is more inwardly situated. This disposition of lobes in our longitudinal images is consistent with our finding from cross-sectional averages that *pf9* is missing density in both the inner and outer domains, but predominantly in the latter. The main issues with regard to the I1 subunit are how its constituent polypeptides are arranged and whether it constitutes a single functional unit. The 1α and 1β heavy chains are present in equal quantities (Piperno and Ramanis, 1991), so it is not obvious how they contribute to the three lobes. Deep-etch electron microscopy of the subunits associated with the 1α/1β heavy chains has revealed structures with two globular heads, each attached to a relatively thick, long stem (ζ/η subunits; Goodenough et al., 1987; Smith and Sale, 1991). Again, the correspondence between these structures and our three lobes is not immediately obvious. Smith and Sale (1991) suggested that the two-headed structure might comprise the entire I1 subunit, with the stems folded up in situ to form a third globular unit. One possibility consistent with this suggestion is that a portion of each heavy chain forms one of the two proximal-most lobes in our model, with the remainder of the heavy chains combined with the 140- and 110-kD intermediate chains (Porter et al., 1992) to form the more distal lobe. However, other arrangements are certainly possible. Future study of revertant strains that rescue a subset of the I1 polypeptides may provide further insight into the arrangement of these polypeptides in situ.

The I2 structures, defined as those associated with the 2

and 2′ heavy chains, have been examined previously by looking either at the additional structures missing in *pf23* relative to *pf30* (an allele of *pf9*; Piperno et al., 1990) or at those missing in *ida4* (Kamiya et al., 1991). In our longitudinal images, we found that the structural deficiency was the same in both of these cases and that it did not fall in a single contiguous region but rather occurred in three separate positions within the 96-nm repeating unit (Fig. 12). These I2 structures comprised three distinct lobes in the inner domain of the inner row and probably a fourth, narrow lobe in the outer domain.

Our longitudinal and cross-sectional averages are in good agreement on several points. First, the amounts of structure associated with the I1 and I2 subspecies are roughly equivalent. The longitudinal averages show three I1 lobes and three or four I2 lobes. Quantitative analysis of cross-sectional averages indicates that the inner arm intensity is reduced by 24% in *pf9* and by an additional 22% in *pf23*, nearly equal amounts. While there are several reasons why the intensities in our cross-sectional averages might not be accurate measures of the true mass of a given structure, it appears that the relative differences from wild-type can provide consistent measures of density lost. Second, both the longitudinal averages and the difference plot between *pf9* and *pf23* cross-sectional averages indicate that densities associated with I2 are located predominantly or exclusively in the inner domain of the inner row, in agreement with Kamiya et al. (1991). Third, the I2 densities are not the sole constituents of the inner domain: one of the I1 lobes and two of the lobes remaining in *pf23* also contribute to the inner domain (stippled lobes in Fig. 12). These lobes correspond to the intensity lost from the inner domain of the *pf9* cross-sectional average (22%), and to the intensity remaining there in *pf23* (35%), respectively. Finally, a cross-sectional average from our one sample of *ida4*, which resembled the images presented by Kamiya et al. (1991), supported the preceding points by showing only a partial loss of intensity in the inner domain (41%).

Our finding that the structural loss in *pf23* was the sum of the separate losses in *pf9* and *ida4* was not a foregone conclusion, because the polypeptide deficiency in *pf23* is greater than the sum of the deficiencies in *pf9* and *ida4*. Polypeptides missing in *pf23* but present in both *pf9* and *ida4* include heavy chain 3′, a portion of heavy chain 2, and several intermediate and light chains (Luck and Piperno, 1989; Piperno et al., 1990; Kamiya et al., 1991). One might have thus expected to see some structure present in both *pf9* and *ida4* but missing from *pf23*. The lack of such structures in our longitudinal images implies that heavy chain 3′ contributes to structures in *pf9* and *ida4* that are equivalent to ones formed by heavy chain 3 (the sole remaining heavy chain) in *pf23*. This implication supports the proposal that heavy chain 3′ substitutes for 3 in the proximal portion of flagella of normal length, and that 3′ is missing in a variety of mutant strains with short flagella simply because the proximal portion of the axoneme is not present (Piperno and Ramanis, 1991; see also Piperno et al., 1990).

It is not obvious how the various I2 structures are related to each other or why they are lost as a unit in *ida4* and *pf23*. Unlike the I1 lobes, which may form a single continuous structure, the I2 lobes may be lost together because they are homologous structures. The possibility of such a homology is suggested by the fact that if there were a third radial spoke in *Chlamydomonas*, then it would be located adjacent to the third I2 lobe, and all three I2 lobes would be adjacent to radial spokes. However, the three I2 lobes cannot all be identically constructed, because both the longitudinal averages and the analysis of serial 24-nm sections indicated that the distal-most lobe is more inwardly located. It is still possible that the two lobes adjacent to the radial spokes are identical. A related question is how the two heavy chains, 2 and 2′, contribute to the various I2 structures. More information on the stoichiometry of the 2 and 2′ heavy chains in wild-type and *ida4* axonemes is needed to address this issue.

Another unresolved issue is the identity of the polypeptide components that form the structures remaining in *pf23* axonemes. Potential candidates include polypeptides associated with inner arm heavy chain 3, polypeptides associated with the radial spoke control system and missing in *pf2*, and polypeptides associated with the nexin linkages between adjacent doublets. Given this range of possibilities, it is inappropriate simply to equate the structures remaining in *pf23* with a dynein arm subspecies formed from heavy chain 3 and associated intermediate and light chains. *Pf2* is missing four axonemal polypeptides (29–65 kD) that form a subset of the radial spoke control system polypeptides identified by suppressor analysis of radial spoke defective mutations (Huang et al., 1982). These polypeptides are postulated to be components of a control system that normally inhibits dynein arm activity in the absence of a signal from the radial spokes, but allows for coordination of dynein arm activity among the outer doublets when radial spokes are present. This control system may be located in the outermost part of the heavily staining crescent in our longitudinal averages (cross-hatched lobe in Fig. 12), because that structure was consistently deficient in *pf2*. This position appears appropriate for a system mediating signals between radial spokes and dynein arms.

The assignment of this control system to the crescent is complicated, however, by the possibility that the nexin link may be part of this structure. Our longitudinal views do not provide information on the nexin link, but our averages from serial 24-nm sections do show a likely candidate for the nexin link: a ridge of density that, in going from proximal to distal, progresses from the B subfiber of the adjacent doublet to the A tubule. This density joins the A-tubule distal to S2, consistent with Goodenough and Heuser's (1989) observations on nexin attachment in *Chlamydomonas* and with a nexin attachment between radial spokes 2 and 3 in the cilia of *Tetrahymena* (Warner, 1983) and in avian sperm flagella (Burgess et al., 1991). If we use the radial spokes to relate positions in the serial cross-sectional averages to positions in the longitudinal averages, we estimate that the corresponding density in the longitudinal averages is from about the distal two-thirds of the crescent to the proximal half of the thickly striped lobe in Fig. 12. This location overlaps with the deficiency in *pf2*. This estimate suggests that the ridge of density may not be nexin, or that the nexin link and the *pf2* deficiencies may both be located in this structure. It is also possible that some of these polypeptides serve overlapping functions; i.e., that the polypeptides deficient in the radial spoke suppressor mutants are actually a subset either

of the inner arm polypeptides or of the nexin polypeptides. Further analysis of other flagellar mutants will be needed to sort out these possibilities.

Relation to Previous Images and Models of Inner Dynein Arms

Our results rule out Kamiya et al.'s (1991) proposal that the I1 subunit forms only an inner projection and that I1 and I2 subunits might thus be arranged side-by-side in parallel rows. Nevertheless, our conclusions are consistent with their images (Kamiya et al., 1991). In particular, their cross-sectional averages show a reduction in inner as well as outer domain intensity in idaA strains (ones missing I1), and variable amounts of density remaining in the outer domain of idaA strains and in the inner domain of *ida4*. Difficulties in interpreting those averages can be attributed to two factors. First, each average is based on eight doublets from a single cross-section, making it hard to assess the true structure in the face of variability both among different axonemes in the same sample and among multiple samples of the same strain. Our grand averages are based on 200–550 doublets and encompass both kinds of variability, thus allowing better comparisons between strains. Second, the photographs of their gray-scale images do not fully convey the magnitude of weak densities. We had similar difficulty in presenting the average of *pf23* in a way that would show the remaining density in the inner lobe. We circumvented this problem by presenting integrated intensities (Fig. 5).

The longitudinal averages presented here clearly show that the I2 subunits do not form a single inner arm structure located between the two radial spokes, as proposed by Piperno et al. (1990). However, their longitudinal images are consistent with ours. In particular, their drawings of inner arm density change from straight in *pf9* to crescent shaped in *pf23*, consistent with loss of the I2 lobe adjacent to S2. We are also in agreement that the gap in structure increases substantially from *pf9* to *pf23*. However, probably because of the difficulty of interpreting unaveraged longitudinal images, Piperno et al. (1990) failed to see that the gap increases at both its distal and proximal ends.

Our longitudinal averages indicate that inner arm structures occur predominantly, but not exclusively, in two separate rows, in partial agreement with Muto et al.'s (1991) model of two rows of inner arms. We can establish a nearly one-to-one correspondence between the arms in their model and the structures in our averages. One discrepancy is that the proximal-most stippled lobe in Fig. 12 seems to correspond to two arms in their model; in fact, this structure does appear to contain two peaks of density in our *pf9* and *pf2* grand averages. The other discrepancy is that nothing in their model corresponds to the thickly striped lobe in Fig. 12, which was variably present in the averages from individual axonemes. This thin structure may have been overlooked or lumped with the proximal-most part of I1, or it may not have been consistently present in the mutant strains that they examined.

Finally, our images of inner dynein structure are at odds with the model of Goodenough and Heuser (1989). Based largely on rapid-freeze, deep-etch micrographs from *Tetrahymena* and *Beröe*, their model shows dynein arms as essentially a single row of lobes, arranged from proximal to distal as a three-headed structure then two two-headed structures. However, the details of their one published image from *Chlamydomonas* (Fig. 15 of Goodenough and Heuser, 1989) appear to be more consistent with our model, and that of Muto et al. (1991), than with their images from *Tetrahymena* or *Beröe*. In particular, distal to radial spoke 1, the lobes there appear to occur in two rows, rather than as two-headed structures in a single row. These observations suggest that inner arm organization may vary among organisms (see also Burgess et al., 1991) and that not all inner arms are arranged as two-headed structures in *Chlamydomonas*. Two additional results are consistent with this possibility. First, neither the lobes lost in *ida4* (the I2 subunits) nor the structures remaining in *pf23* (which must include the I3 subspecies) show a two-headed arrangement. Second, only single-headed units are isolated from fractions containing dynein heavy chains other than the $1\alpha/1\beta$ subunit (Goodenough et al., 1987; Smith and Sale, 1991).

The application of the methods described here to a wider range of mutant axonemes, and increased resolution in the analysis of dynein heavy chains, will help to resolve many of the issues discussed above. In any case, the dynein inner arm structures in *Chlamydomonas* now show a complexity of organization commensurate with the intricacies of its swimming behavior.

We thank Guy Vigers and Sam Mitchell for their contributions to the early development of the computer hardware and the image-averaging procedures, Mary Morphew for her excellent technical assistance, and Susan Dutcher for support and for comments on the manuscript. The *ida1* and *ida4* strains were generously provided by Dr. R. Kamiya.

This work was supported by grant RR-00592 from the National Institutes of Health, and by National Science Foundation grants DCB 9005079 to M. E. Porter and DCB 8518224 to Susan K. Dutcher and M. E. Porter.

Received for publication 21 February 1992 and in revised form 21 May 1992.

Note Added in Proof: Preliminary study of other mutant strains has revealed possible subdivisions of each of the structures remaining in *pf23* (the lobes labeled 8, 9, and 10 in Fig. 11 *H*), which may require small changes in the model presented here. In particular, lobe 5 may extend more proximally, over the inner tip of lobe 8, and the inner tip of lobe 9 may be missing in *pf2*.

References

Brokaw, C. J., and R. Kamiya. 1987. Bending patterns of *Chlamydomonas* flagella IV. Mutants with defects in inner and outer dynein arms indicate differences in dynein arm function. *Cell Motil. Cytoskeleton.* 8:68–75.

Burgess, S. A., D. A. Carter, S. D. Dover, and D. M. Woolley. 1991. The inner dynein arm complex: compatible images from freeze-etch and thin section methods of microscopy. *J. Cell Sci.* 100:319–328.

Frank, J., W. Goldfarb, D. Eisenberg, and T. S. Baker. 1978. Reconstruction of glutamine synthetase using computer averaging. *Ultramicroscopy.* 3: 283–290.

Goodenough, U. W., and J. E. Heuser. 1989. Structure of the soluble and *in situ* ciliary dyneins visualized by quick-freeze deep-etch microscopy. *In* Cell Movement. Vol. 1. F. D. Warner, P. Satir, and I. R. Gibbons, editors. Alan R. Liss, Inc., New York. 121–140.

Goodenough, U. W., B. Gebhart, V. Mermall, D. R. Mitchell, and J. E. Heuser. 1987. High pressure liquid chromatography fractionation of *Chlamydomonas* dynein extracts and characterization of inner arm dynein subunits. *J. Mol. Biol.* 194:481–494.

Hoops, H. J., and G. B. Witman. 1983. Outer doublet heterogeneity reveals structural polarity related to beat direction in *Chlamydomonas* flagella. *J. Cell Biol.* 97:902–908.

Huang, B., G. Piperno, and D. J. L. Luck. 1979. Paralyzed flagella mutants of *Chlamydomonas reinhardtii*. *J. Biol. Chem.* 254:3091–3099.

Huang, B., Z. Ramanis, and D. J. L. Luck. 1982. Suppressor mutations in *Chlamydomonas* reveal a regulatory mechanism for flagellar function. *Cell.* 28:115–124.

Kamiya, R., E. Kurimoto, H. Sakakibara, and T. Okagaki. 1989. A genetic ap-

proach to the function of inner and outer arm dynein. *In* Cell Movement. Vol. 1. F. D. Warner, P. Satir, and I. R. Gibbons, editors. Alan R. Liss, Inc., New York. 209–218.

Kamiya, R., E. Kurimoto, and E. Muto. 1991. Two types of *Chlamydomonas* flagellar mutants missing different components of inner-arm dynein. *J. Cell Biol.* 112:441–447.

King, S. M., and G. B. Witman. 1989. Molecular structure of *Chlamydomonas* outer arm dynein. *In* Cell Movement. Vol. 1. F. D. Warner, P. Satir, and I. R. Gibbons, editors. Alan R. Liss, Inc., New York. 61–75.

Luck, D. J. L., and G. Piperno. 1989. Dynein arm mutants of *Chlamydomonas*. *In* Cell Movement. Vol. 1. F. D. Warner, P. Satir, and I. R. Gibbons, editors. Alan R. Liss, Inc., New York. 49–60.

McDonald, K., D. Mastronarde, E. O'Toole, R. Ding, and J. R. McIntosh. 1991. Computer-based tools for morphometric analysis of mitotic spindles and other microtubule systems. *EMSA Bull.* 21:47–53.

Muto, E., R. Kamiya, and S. Tsukita. 1991. Double-rowed organization of inner dynein arms in *Chlamydomonas* flagella revealed by tilt-series thin-section electron microscopy. *J. Cell Sci.* 99:57–66.

Piperno, G., and Z. Ramanis. 1991. The proximal portion of *Chlamydomonas* flagella contains a distinct set of inner dynein arms. *J. Cell Biol.* 112: 701–709.

Piperno, G., Z. Ramanis, E. F. Smith, and W. S. Sale. 1990. Three distinct inner dynein arms in *Chlamydomonas* flagella: molecular composition and location in the axoneme. *J. Cell Biol.* 110:379–389.

Porter, M. E., J. M. Power, and S. K. Dutcher. 1992. Extragenic suppressors of paralyzed flagellar mutations in *Chlamydomonas reinhardtii* identify loci that alter the inner dynein arms. *J. Cell Biol.* 118:1163–1176.

Smith, E., and W. S. Sale. 1991. Microtubule binding and translocation by inner dynein arm subtype I1. *Cell Motil. Cytoskeleton.* 18:258–268.

Warner, F. D. 1983. Organization of interdoublet links in *Tetrahymena* cilia. *Cell Motil.* 3:321–332.